Structural, catalytic/redox and electrical characterization of systems combining Cu–Fe with CeO_2 or $Ce_{1-x}M_xO_{2-\delta}$ (M = Gd or Tb) for direct methane oxidation

A. Hornés [a,*], G. Munuera [b], A. Fuerte [c], M.J. Escudero [c], L. Daza [a,c], A. Martínez-Arias [a,**]

[a] Instituto de Catálisis y Petroleoquímica (CSIC), C/ Marie Curie 2, Campus de Cantoblanco, 28049 Madrid, Spain
[b] Universidad de Sevilla, C/ Profesor García González s/n, Departamento de Química Inorgánica, 41012 Sevilla, Spain
[c] CIEMAT, Avda, Complutense 22, 28040 Madrid, Spain

ARTICLE INFO

ABSTRACT

The present work analyses bimetallic Cu–Fe formulations combined with CeO_2 or other structurally related mixed oxides resulting from doping of the former with Gd or Tb, focusing to its possible use as anodes of solid oxide fuel cells (SOFC) for direct oxidation of methane. The main objective is the characterization of the various formulations at structural level as well as with regard to redox changes taking place in the systems upon interaction with methane, in order to evaluate the effects induced by the presence of the mentioned dopants. In the same sense, an analysis of thermal expansion and electrical properties of the systems as well as their chemical compatibilities with several electrolytic materials is performed, considering its possible implantation in SOFC single cells. For the mentioned purposes, the systems have been analysed by means of CH_4-TPR tests subsequently followed by TPO tests, as well as by XRD, Raman and XPS, with the aim of exploring structural and redox changes produced in the systems and the formation of carbon deposits during interaction with methane. The results reveal significant modifications in the structural, catalytic/redox and electrical properties of the systems as a function of the presence of Fe and/or Gd and Tb dopants in the formulation.

1. Introduction

Solid oxide fuel cells (SOFC) are galvanic devices most interesting from environmental and energetic points of view due to their high efficiency for conversion from chemical to electrical energy and their high versatility towards employment of various types of fuels [1]. Classical systems of this type involve the employment of thin YSZ electrolytes with an anode typically based on Ni-YSZ cermets and can attain an energetic efficiency close to 70% operating at relatively high temperature (800–1000 °C) with hydrocarbon reforming mixtures as fuel [1–3]. This efficiency can be theoretically increased by employing direct hydrocarbon oxidation conditions instead of fuel mixtures resulting from reforming [4]. However, the classical anode of nickel could easily be deactivated under those conditions as a consequence of the formation of carbonaceous deposits due to the relatively good activity of nickel for hydrocarbon cracking [5–8]. Different alternatives were devel-

oped in this respect to overcome such deactivating effect. Murray et al. successfully operated a cell on dry methane by employing a nickel-containing ceria-based anode at relatively low reaction temperature (650 °C) [6]. In turn, such ceria-containing anode could in principle be compatible with electrolytes able to operate at intermediate temperatures (500–700 °C) like gadolinium-doped ceria (CGO) [1].

However, the nickel-based anode can be less suitable when less refractory, easier to be cracked hydrocarbons are employed as fuel [5,7,8]. A more versatile alternative was developed by Gorte, Vohs and colleagues that consisted in employing anodes based on mixtures between copper and cerium oxide [5,7,9–16]. Such configuration has demonstrated to be able to employ a large diversity of hydrocarbon fuels (methane or longer chain ones and even aromatics) under direct oxidation conditions and displaying a reasonable stability [4,7,11]. However, although it could in principle perform well at intermediate temperatures, the copper anode can present several limitations related to its poor thermal stability as a consequence of the low melting point of copper, which can make difficult the fabrication of Cu cermets and affect the anode stability when operating at high temperature [16,17], as well as to its poor performance for hydrocarbon activation [4,16]. An interesting alternative in this sense

consists in employing bi- or multi-metallic anode formulations [4,18,19].

In this context, the present work explores the properties of bimetallic Cu–Fe configurations, considering the higher thermal stabilities and chemical reactivity of iron with respect to copper, for direct methane oxidation, using a basic copper–ceria configuration as the starting reference material. The effects of the modifications of the properties of ceria that occur upon doping with Gd and Tb [20] are also analysed; in this respect, previous work of our group demonstrated that doping of ceria with Tb induces changes in the type of conductivity and makes the system more stable towards thermal sintering [21]. The work complements the results of previous analysis in which Cu–Ni bimetallic systems, instead of Cu–Fe ones, were examined with respect to their main physicochemical properties for methane direct oxidation [22,23]. Within mentioned context, materials synthesized by a microemulsion method were examined by X-ray diffraction (XRD), X-ray photoelectron spectroscopy (XPS) and specific surface area measurements (S_{BET}) and analysed with respect to their redox/catalytic properties by means of temperature programmed reduction (TPR) tests under dry methane; supplementary analysis of chemical compatibility with different conventional electrolytic materials as well as thermal expansion coefficient and electrical conductivity both under air or diluted H_2 is also undertaken. The work will explore also with temperature programmed oxidation (TPO), Raman and XPS the generation of carbon deposits during direct hydrocarbon interaction and the chemical changes produced by them on the composite material; these are expected to affect the anode components and the SOFC performance. In general, such deposits will poison the anode, although in some bimetallic Cu–M configurations they have displayed positive effects attributed to an increase of electrical conduction that would be due to an enhanced connectivity at microscopic level between metal particles in the anode [4].

2. Experimental

2.1. Materials

Systems combining Cu–Fe with CeO_2, $Ce_{0.9}Gd_{0.1}O_{2-x}$ or $Ce_{0.8}Tb_{0.2}O_{2-y}$ were prepared by coprecipitation within reverse microemulsions. For this purpose, two reverse microemulsions, of similar characteristics concerning the volumes employed of organic (n-heptane) and aqueous phases as well as of surfactant (Triton X-100) and co-surfactant (1-hexanol), were prepared; details of the method can be found elsewhere [24]. The first one contained in its aqueous phase the dissolved (nitrate) salts of Ce, Gd, Tb, Cu or Fe while the second one contained in its aqueous phase a dissolved base (tetramethyl ammonium hydroxide or TMAH) which is employed as precipitating agent. Mixing both microemulsions produces the precipitation of the cations and after separation of the solid by centrifugation and decantation, the resulting solid is rinsed with methanol and dried for 24 h at 100 °C. The resulting material is then calcined under air initially at 500 °C during 2 h and finally at 950 °C during 2 h, employing relatively slow heating ramps of 2 °C min^{-1}. Samples with total metal (Cu + Fe) loading of 40 wt.% (with Cu/Fe = 1/1 atomic ratios) have been prepared (i.e. corresponding to atomic ratio of (Cu + Fe)/Ce ≈ 2). Chemical analyses of the samples by ICP-AES demonstrated quantitative precipitation in any of the samples, the actual contents of any component being the same (within experimental error) as the nominal values employed. The samples will be denoted hereafter as CuFe-C, CuFe-CG and CuFe-CT depending on whether the support material is CeO_2, $Ce_{0.9}Gd_{0.1}O_{2-x}$ or $Ce_{0.8}Tb_{0.2}O_{2-y}$, respectively.

2.2. Techniques

S_{BET} determination was made from curves of adsorption/desorption of N_2 at −196 °C over the samples outgassed at 140 °C using a Micromeritics ASAP 2100 equipment. S_{BET} values obtained evidenced a significant sintering of samples calcined at 950 °C, experimental values obtained being in any case below detection limit of the technique.

Powder XRD patterns of the samples were recorded on a Seifert XRD 3000P diffractometer using nickel-filtered Cu Kα radiation operating at 40 kV and 40 mA, using a 0.02° step size and 2 s counting time per point.

XPS spectra were recorded with a Leybold-Heraeus spectrometer equipped with an EA-200 hemispherical electron multichannel analyzer (from Specs) and a 120 W, 30 mA Mg Kα X-ray source. The samples (0.2 mg) were slightly pressed into a small (4 mm × 4 mm) pellet and then mounted on the sample rod and introduced into the pretreatment chamber of the spectrometer where they were briefly outgassed and then moved into the ion-pumped analysis chamber where it was further outgassed until a pressure less than 2×10^{-9} Torr was attained (2–3 h). This low pressure was maintained during all the data acquisition by ion pumping of the chamber. After each treatment, XP spectra in the relevant energy windows were collected for 20–90 min, depending on the peak intensities, at a pass energy of 44 eV (1 eV = 1.602×10^{-19} J), which is typical of high resolution conditions. The intensities were estimated by calculating the integral of each peak after subtraction of an S-shaped Shirley-type background with the help of UNIFIT for Windows (version 3.2) software [25]; atomic ratios were then derived using the appropriate experimental sensitivity factors. All binding energies (BE) were referenced to the Ce(3d) u‴ line at 917.0 eV which, as we have previously shown [26], gives a value of 284.6 ± 0.1 eV for the adventitious graphitic C(1s) line.

Raman spectra were collected at room temperature using a Renishaw Dispersive System 1000 equipped with a cooled CCD detector and holographic Notch filter. The samples were excited with the red laser line (632.8 nm) and the spectral resolution was 3 cm^{-1}.

TPR tests under diluted dry methane (5% CH$_4$/He) were done in a quartz flow microreactor filled with about 500 mg of sample and employing 150 mL min^{-1} total flow. Heating ramps of 10 °C min^{-1} from 30 to 900 °C, maintaining finally this temperature for 2 h under the reactant mixture (enough in all cases for achieving stabilization of the reaction products), were used. Subsequently, the sample was cooled under the same flow and after extensive purging under He at 30 °C they were subjected to a temperature programmed oxidation (TPO) test under 5% O_2/He (using the same flow rate as for the TPR tests) up to 900 °C (10 °C min^{-1} ramp), keeping then this temperature until products stabilization. Gases evolving from the reactor were analysed with a Pfeiffer Omnistar quadrupolar mass spectrometer.

Thermal expansion coefficients (TEC) were measured on an alumina dilatometer Linseis L75/1550, heating from room temperature to 750 °C at a rate of 5 °C min^{-1} both under air and 10% H_2/N_2. Prior to these measurements, samples were cold-pressed into pellets (10 mm diameter and 0.9 mm thickness) at a pressure of 2 ton cm^{-2} and calcined for 2 h at 950 °C.

The electrical conductivity of the systems was measured in air by impedance spectroscopy and in 10% H_2 by the four point DC method in the temperature range 200–750 °C. The impedance measurements were carried out on a pellet coated with platinum paste on each face and fired at 900 °C for 1 h. The impedance data were recorded by an AUTOLAB system (PGSTAT30 and FRA2 module, Eco Chemie) over the frequency range from 1 MHz to 10 mHz at open circuit with a signal amplitude of 100 mV. A dense bar of the compound (20 mm × 5 mm × 1.5 mm) was prepared for the DC conductivity measurements. The electrical contacts were ensured
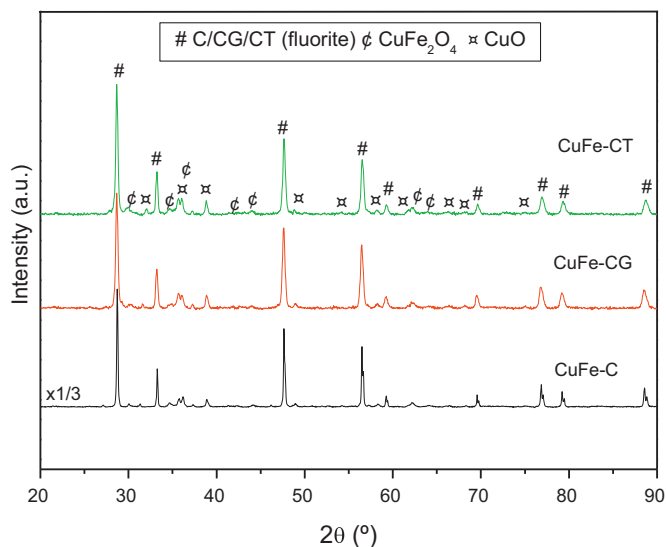
Fig. 1. X-ray diffractograms of the indicated samples calcined under air at 950 °C.
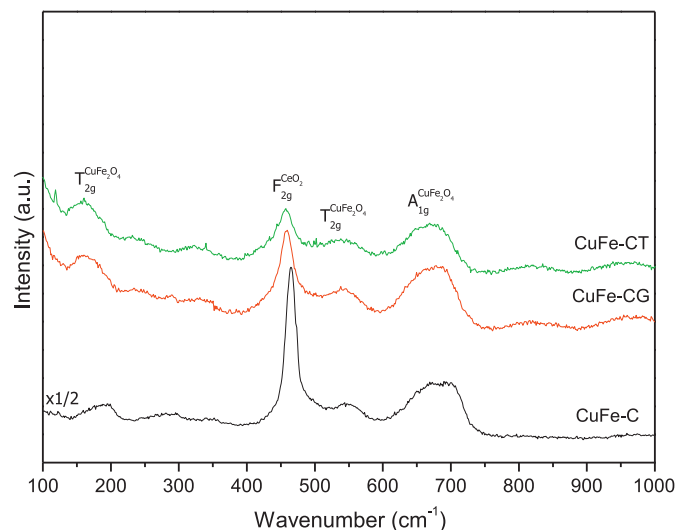

Fig. 2. Raman spectra of the indicated samples calcined under air at 950 °C.

with gold wire and a gold conductor paste. A current load was applied by a Dual Output DC Power Supply (Agilent E3646A) and the potential drop recorded by a Digital Multimeter (Agilent E34401A). Supplementary scanning electron microscopy (SEM) analysis of the materials examined during these tests of electrical properties was done with a Hitachi-S-2500 microscopy.

Chemical compatibility tests were carried out with the anode systems and materials commonly used as SOFC electrolyte such as 8YSZ, LSGM ($La_{0.9}Sr_{0.1}Ga_{0.8}Mg_{0.2}O_{3-\delta}$) and CGO ($Ce_{0.8}Gd_{0.2}O_{2-\delta}$); prefixes Y, L and C will be employed, respectively, in the nomenclature of mixtures including these electrolytes. Equal amount of anode powders and electrolyte were thoroughly ground in an agate mortar and put into a quartz reactor. The mixture was fired in humidified hydrogen (3% H_2O) for 50 h at 750 °C. After completion, XRD patterns were recorded following the same conditions described above.

3. Results and discussion

3.1. Structural analysis

The structural properties of the anode formulations in the initial after calcination at 950 °C state have been examined by XRD. The X-ray diffractograms display peaks due to the fluorite phase of either CeO_2 or Gd- or Tb-doped ceria [27,28] (Fig. 1). Lattice parameters estimated from the diffractograms for this phase are of 5.411, 5.413 and 5.399 Å for CuFe-C, CuFe-CG and CuFe-CT samples, respectively, fairly independent on the presence of Cu or Fe in the formulation, consistent with the formation of the corresponding doped phases in the fluorite component. In the case of the Tb-containing samples, the fluorite lattice parameter value indicates the presence of both Tb^{3+} and Tb^{4+} states, in agreement with previous analysis [28]. Thus, assuming that Vegard's rule is obeyed within a series of CT mixed oxides and that 5.213 Å is the lattice parameter for TbO_2 (and 5.411 Å for CeO_2), a lattice parameter of 5.371 Å would be expected for this mixed oxide if the whole terbium in CuFe-CT would be as Tb^{4+} (considering an atomic fraction Tb/(Ce + Tb) = 0.2, according to chemical analysis). In turn, if the whole terbium would be as Tb^{3+}, an expansion (with respect to CeO_2) to 5.418 Å in the lattice parameter would be expected, assuming a lattice expansion of 0.0375 Å per atomic fraction of Tb^{3+} doping the CeO_2 lattice [29]. On this basis, assuming a linear behaviour in the degree of lattice expansion with increasing the relative amount of Tb^{3+} (as generally

observed to occur with other trivalent dopants [29]), about 60% of the terbium is estimated to appear as Tb^{3+} in CuFe-CT. It can be noted that such value makes the two samples doped with gadolinium and terbium practically comparable in terms of the amount of dopant cations in the +3 valence state present in the initial samples.

The average sizes of the fluorite crystals, determined from XRD linewidths using Scherrer's formula are of ca. 61, 29 and 34 nm for CuFe-C, CuFe-CG and CuFe-CT samples, respectively, evidencing a beneficial effect of doping with Gd or Tb on decreasing particle size of the fluorite phase. Concerning phases related to the Cu and Fe components, tenorite CuO and $CuFe_2O_4$ are detected in all cases with relatively small differences being observed as a function of Gd or Tb presence both in terms of lattice parameters or crystal size (around 30 nm for the $CuFe_2O_4$ phase and 63, 46 and 69 nm for CuO in CuFe-C, CuFe-CG and CuFe-CT samples, respectively).

XRD results are consistent with those obtained by Raman spectroscopy (Fig. 2). These show mainly a strong peak at ca. 464 cm^{-1} corresponding to the triply degenerate F_{2g} mode of fluorite CeO_2 or related Gd- or Tb-doped fluorite structure, which is the only one allowed in first order for this phase [30]. A small red shift in such peak position is observed for CuFe-CG and CuFe-CT, consistent with effects expected upon respective doping of the ceria lattice and as a consequence of lattice contraction [30], in agreement with XRD results. In addition, a broad peak extending between 500 and 700 cm^{-1} is expected which has been related to oxygen vacancies present in the samples as a consequence of Gd^{3+} or Tb^{3+} substitutionally present in the fluorite lattice and charge compensation requirements [28,30]; nevertheless, such peak apparently overlaps with another one related to $CuFe_2O_4$ which in turn exhibits peaks at ca. 190 cm^{-1} and between 650 and 700 cm^{-1}, in agreement with previous assignment [31]. Smaller peaks or shoulders at ca. 290, 340 and 625 cm^{-1} corresponding to the three Raman active modes (Ag + 2Bg), expected for tenorite CuO [32], appear also present in the spectra. In turn, XPS examination of the initial materials display a small copper enrichment with respect to iron at the sample surface; valence states detected by XPS are consistent with XRD and Raman results, showing all components in their highest oxidation states expected within corresponding oxide structures (Cu^{2+}, Fe^{3+}, Ce^{4+}, Tb^{4+}/Tb^{3+} and Gd^{3+}).

3.2. Catalytic/redox properties

Concerning the analysis of redox/catalytic properties on the basis of CH_4-TPR tests, Fig. 3 displays the evolution of the gases
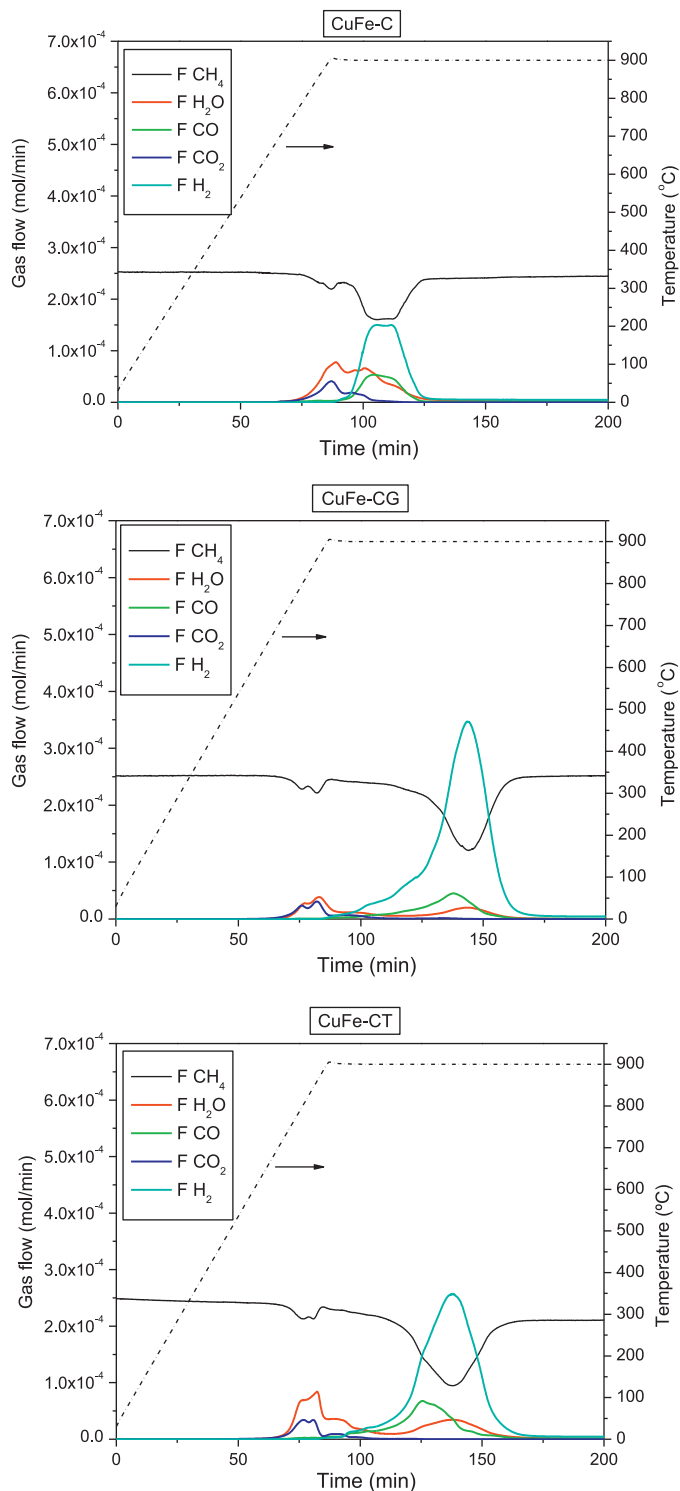
Fig. 4. Evolution of CO_2 during TPO tests performed over the indicated samples subsequently to CH_4-TPR tests.

beneficial effects of Gd or Tb doping on this parameter too. In any of the cases, full CH_4 oxidation, yielding CO_2 and H_2O is the first reaction taking place. As oxygen in the samples is consumed, such reaction becomes extinguished being replaced by partial oxidation processes yielding $CO + H_2$ or $CO + H_2O$. Differences in such partial oxidation processes are evidenced by values of overall selectivity to H_2 detected during the oxidation processes, which also increases with Gd or Tb presence in the materials (70.7%, 81.3% and 83.3% for CuFe-C, CuFe-CG and CuFe-CT, respectively). It is also apparent in this sense that the relative amount of H_2 produced with respect to $CO + CO_2$ is higher in the presence of Gd or Tb, suggesting that methane decomposition (or pyrolysis) to yield $C + H_2$ is most favoured for these materials. Such formation of carbon deposits could in any case explain final deactivation of the catalysts. It is also noteworthy the increase in the stability experimented by the mixed oxide due to the presence of Gd or Tb which causes a delay in H_2 production onset (mostly related to methane pyrolysis). This fact suggests that a modification of the interaction between metallic and ceramic phases is taking place when these lanthanide dopants are present.

Carbon deposits formation has been evidenced by TPO measurements performed at the end of the CH_4-TPR tests after cooling under

Fig. 3. Evolution of gases detected during CH_4-TPR tests over the indicated samples. Temperature evolution (right scale) is shown as dotted line.

detected for the three samples. Significant differences are found as a function of the presence of Gd or Tb dopants in the fluorite phase. First to be noted, an appreciable increase of overall CH_4 conversion (based on analysis of integrated areas of the CH_4 evolution curves) is observed in the presence of those dopants. While 5.6% conversion is attained for CuFe-C, Gd or Tb presence increase such value to 7.7% and 8.1%, respectively. Another remarkable difference is related to onset of CH_4 oxidation, which is produced at 700, 575 and 557 °C for CuFe-C, CuFe-CG and CuFe-CT, respectively, thus revealing the
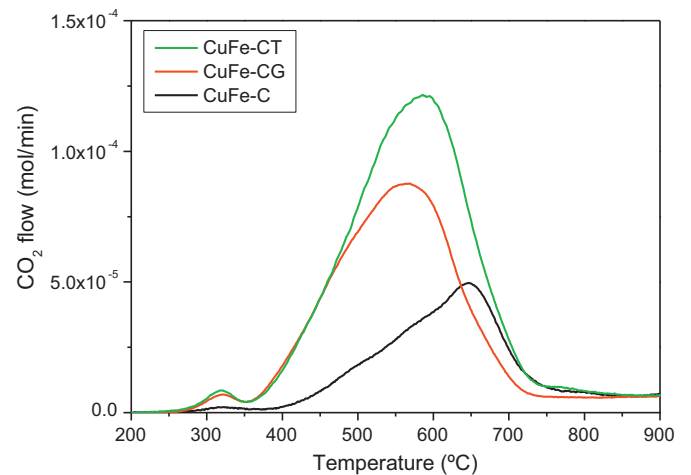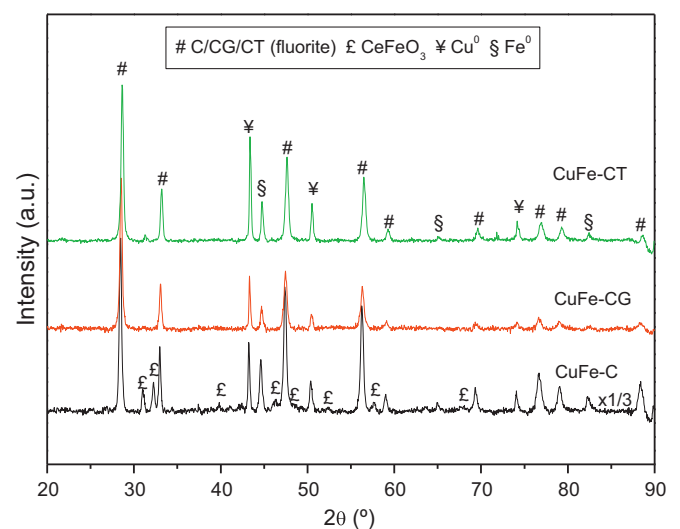

Fig. 5. X-ray diffractograms of the indicated samples after CH_4-TPR tests up to 900 °C and cooling under inert gas and exposure to air at room temperature.
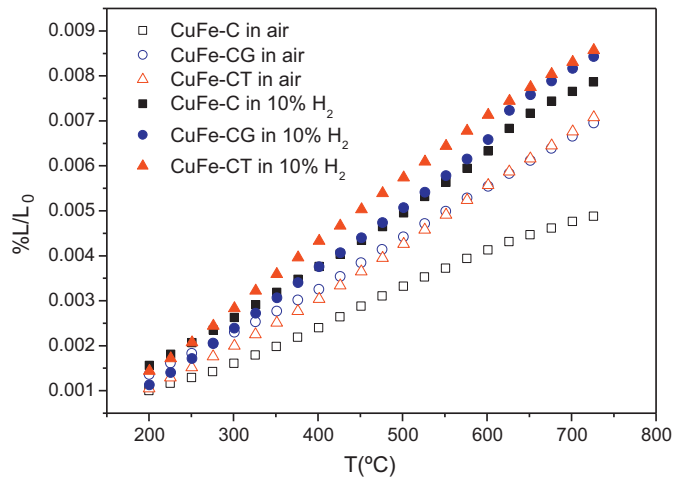
Fig. 6. Thermal expansion curves for Cu–Fe systems in air and 10% H_2/N_2.

inert gas, as shown in Fig. 4. It is observed that the overall amount of carbon deposits formed increases as CuFe-C < CuFe-CG < CuFe-CT, thus revealing that doping of the fluorite phase favours also methane decomposition reaction, in agreement also with results exposed in the former paragraph. It is also likely that in global terms a relatively higher amount of oxygen can be released from CuFe-C than from the other two systems, in accordance with generation of relatively higher amounts of $CO_2 + H_2O$ during the CH_4-TPR tests (Fig. 3), which can help to prevent generation of carbonaceous deposits over that system. Concerning the nature of the carbonaceous deposits formed, those appearing below ca. 400 °C (most favoured in the presence of Gd or Tb) could be related to carbon species well dispersed (atomically) over the metallic particles, so-called C_α [33–35]. Polymerization of the former could give rise to laminar carbon, so-called C_β, which would evolve at somewhat higher temperature around 500 °C [34,35]. Carbon filaments, whose oxidation temperature varies with their respective diameter, could evolve above ca. 550 °C [34–36]. Finally, graphitic carbon can also be formed and is expected to oxidise above ca. 650 °C [34–36]. In general terms, on the basis of these attributions, the presence of Gd or Tb in the materials apparently favour generation of a relatively higher amount of more labile carbon species of filamentous, polymerized or atomically dispersed types with respect to graphitic carbon whose formation appears more favoured in the absence of such dopants. The different nature of these carbon species also evidences the modification of metallic–ceramic phases interaction as a function of the presence of Gd or Tb dopants in the fluorite phase.

Characterization of the materials after the CH_4-TPR tests has been also performed by XRD (after cooling under inert gas and exposure to air at room temperature), as shown in Fig. 5. These evidence the generation of metallic states of the two metals with no evidence of alloy generation in any case. Main differences between the samples are related to formation of cerium orthoferrite ($CeFeO_3$) in the absence of Gd or Tb (Fig. 3), which evidences that the latter dopants act as stabilizers for iron and cerium preventing their loss in the form of such mixed oxide phase. This is in agreement with XPS results showing the presence of Ce^{3+} contributions only for sample CuFe-C while all cerium appears as fully oxidised (as a consequence of exposure to air) in CuFe-CG and CuFe-CT. Analysis of crystal size of the fluorite phase or metals reveal that no particular sintering is produced with respect to initial (oxidised) states in any of the components; about 30 nm crystals are observed in any of the cases for the fluorite phase while metallic copper and iron display crystals between 46 and 63 nm, and 29 and 68 nm, respectively. Relatively higher amounts of metal-
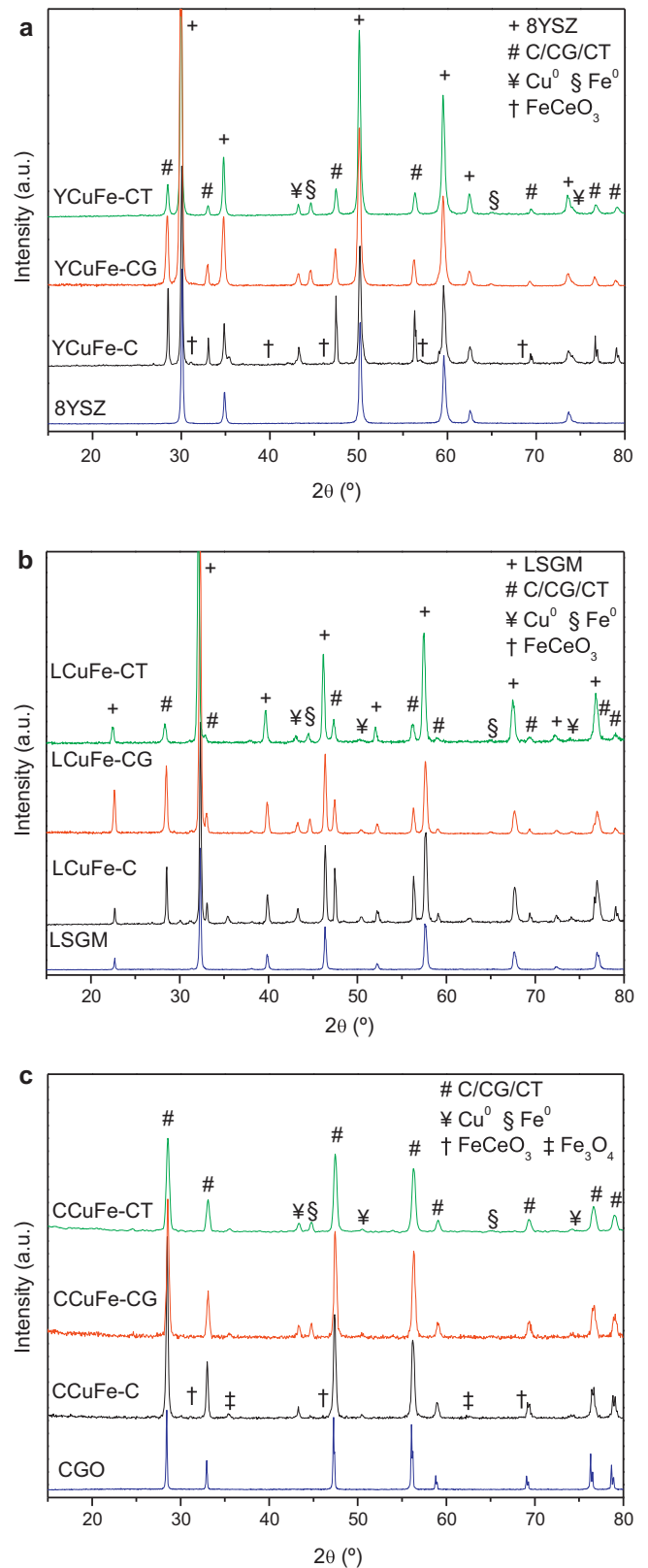

Fig. 7. XRD patterns for chemical compatibility tests between CuFe systems and electrolytes: (a) 8YSZ (YCuFe-samples); (b) LSGM (LCuFe-samples) and (c) CGO (CCuFe-samples).
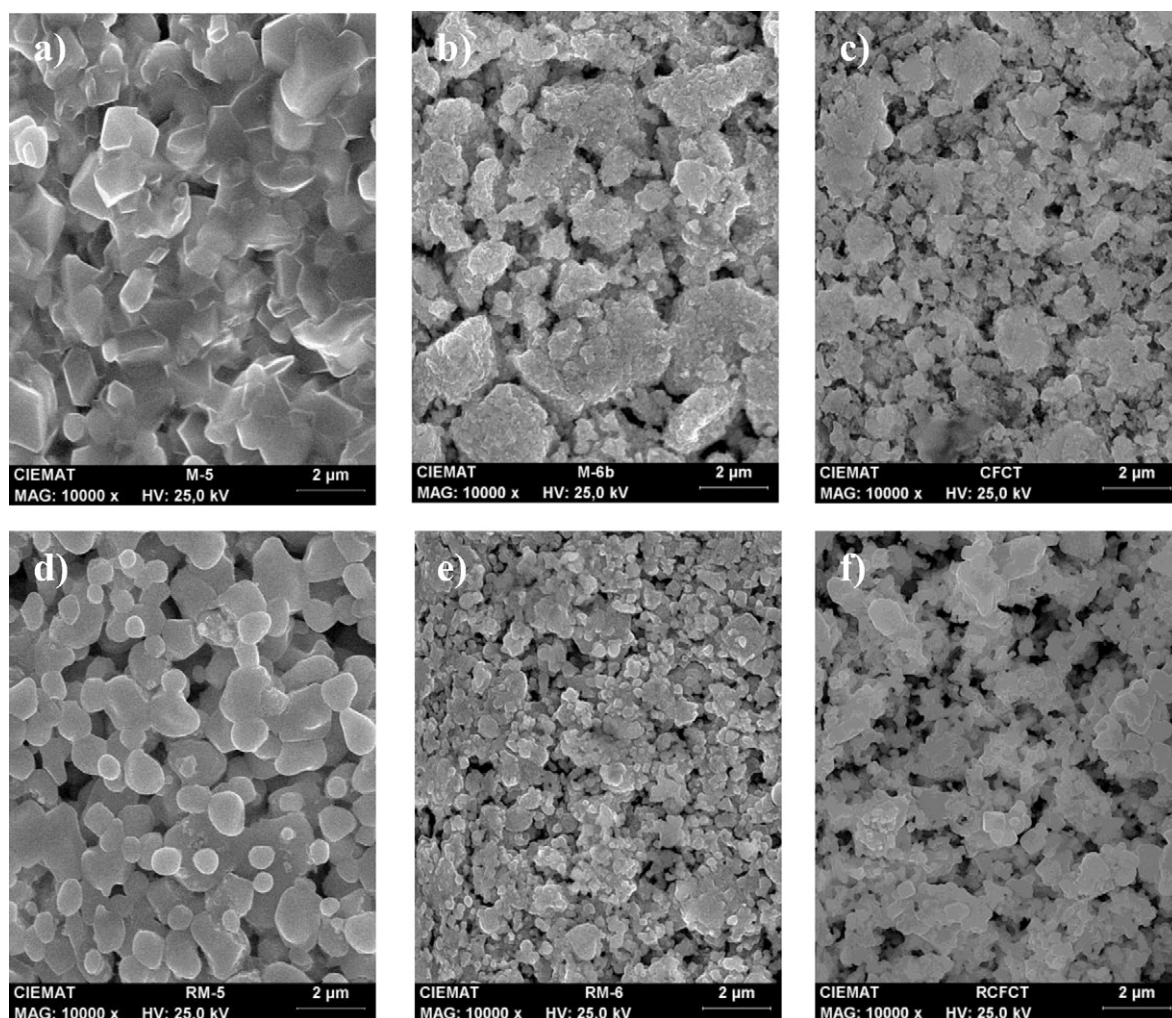
Fig. 8. SEM micrographs of the bimetallic CuFe systems: in air (a) CuFe-C; (b) CuFe-CG; (c) CuFe-CT. In 10% H_2; (d) CuFe-C; (e) CuFe-CG and (f) CuFe-CT.

lic particles are nevertheless detected in the presence of Tb. More important changes are however, detected by XPS analysis of the samples subjected to CH_4-TPR (and cooled under inert gas and exposed to air at room temperature). Thus, an appreciable increase in the Cu/(Cu + Fe) ratio is detected with respect to values detected for the initial samples calcined under air at 950 °C. This suggests that core–shell bimetallic particles in which copper has been segregated to the surface could be formed during reduction under CH_4. In turn, an important decrease in (Cu + Fe)/(Ce + M) – M = Gd or Tb – ratio is also produced during CH_4-TPR test (from 1.84 to 1.41 in the CuFe-C sample; a similar trend was observed for the other two samples although reliable values could not be obtained for them). On the whole, these results suggest that in addition to reduction processes evidenced by XRD or XPS, decoration of the metallic particles by reduced ceria – or doped ceria – subspecies, so-called SMSI effect, could be taking place. Alternatively, effects of carbon deposition which could selectively cover the metallic particles could be pointed out to explain these results.

3.3. Analysis of thermal and chemical compatibility with common electrolytes

The influence of gadolinium or terbium doping of ceria in the thermal expansion coefficients (TECs) was studied for the bimetallic Cu–Fe systems. The thermal expansion curves, in both air and 10% H_2, in the temperature range from 200 to 750 °C are illustrated

in Fig. 6. The average thermal expansion coefficients for all compositions obtained from the corresponding slope of the lines are listed in Table 1. The TEC values are between 7.82 and 11.74×10^{-6} K^{-1} under air and between 12.44 and 14.27×10^{-6} K^{-1} under 10% H_2/N_2. The higher TEC values obtained in reducing atmosphere can be ascribed to the lower cohesive forces expected to be present in the reduced lanthanide oxide phase (due to the decrease in both average cation charge and number of anions), as also noted in previous analyses of CuNi (i.e. without Fe) systems analogous to the ones here studied [23]. The incorporation of Gd and Tb in the ceria structure produces an increase in the TEC values, which may be attributed to the increase in the number of oxygen vacancies and the simultaneous decrease in average cation charge that occur upon substitution of Ce^{4+} by Gd^{3+} or Tb^{3+} [23]. Comparing the effect of the two dopants, the TEC values obtained with Tb are higher in the oxidised samples and lower under reducing condition; this arises probably from a complex interplay between the higher Tb dopant concentration (20 at.% for Tb and 10 at.% for Gd) and the differences

Table 1
TEC values for the bimetallic Cu–Fe systems in air and 10% H_2.

Sample	TEC (K^{-1}) in air	TEC (K^{-1}) in 10% H_2
CuFe-C	7.82×10^{-6}	12.44×10^{-6}
CuFe-CG	10.81×10^{-6}	14.27×10^{-6}
CuFe-CT	11.74×10^{-6}	13.86×10^{-6}

in ionic radii between Gd^{3+}, Tb^{3+} and Tb^{4+}. Except for CuFe-C in air, the TEC values obtained are close to those of 8YSZ, LSGM and CGO ($\approx 10.5 \times 10^{-6}$, 11.8×10^{-6} and $12.9 \times 10^{-6}\,K^{-1}$, respectively), electrolytes commonly used in SOFC and IT-SOFC.

As important as a good electrode–electrolyte thermal compatibility in order to avoid mechanical problems, the chemical compatibility between electrode materials and electrolyte is a prerequisite to any further cell testing. Indeed, the formation of reaction products at the electrode/electrolyte interface could be detrimental to the cell efficiency. The cationic inter-diffusion has to be limited in order to prevent the degradation in electrode and electrolyte materials properties. In this sense, reactivity studies were carried out to assess the interaction between the anode materials and electrolytes commonly used in SOFC such as 8YSZ, LSGM and CGO. XRD patterns for mixtures anode/electrolyte after long heat-treatment with humidified hydrogen can allow dismissing any chemical reaction between electrode and electrolyte materials (Fig. 7), providing evidence of good chemical compatibility between them. The main noticeable change after treatment was the total reduction of metallic oxides (CuO and $CuFe_2O_4$) present on the surface before beginning this treatment with no evidence of alloy generation. Diffraction peaks attributed to Cu^0 and Fe^0 appear together with those for cubic phases of cerium-doped oxide and 8YSZ or the perovskite phase for LSGM.

As has been previously observed (Fig. 5), a new phase of cerium orthoferrite ($CeFeO_3$) is formed in the reduced CuFe-C samples (YCuFe-C and CCuFe-C, Fig. 7a and c). For LCuFe-C characteristic diffraction peaks for the perovskite phase of LSGM overlap those of $CeFeO_3$ (Fig. 7c). Furthermore, it should be noted that in all electrode/electrolyte chemical compatibility samples (Fig. 7a–c), specially for those including CuFe-C material, an appreciable increase in the Cu/(Cu + Fe) ratio is detected. The formation of core–shell bimetallic particles, under reducing conditions, in which copper has been segregated to the surface could be responsible for this phenomenon. On the other hand, cationic interdiffusion across electrode/electrolyte interface has been discarded on the basis of SEM–EDX analysis (data not shown).

3.4. Analysis of electrical conductivity

Prior to analysis of electrical properties of the anode formulations, the samples were examined by SEM in order to study their morphological characteristics, taking into account the relevancy these could have on the macroscopic electrical conductivity. SEM studies reveal that the doping of ceria with Gd or Tb causes important morphological changes (Fig. 8). The CuFe-C sample with undoped ceria shows a more homogeneous microstructure and a highest particle size around 2 μm. In air, the incorporation of Gd or Tb in the structure leads to an increase of porosity, a reduction of particle sizes and the formation of agglomerates which become more apparent for the CuFe-CT sample. After their reduction, in 10% H_2 at 750 °C for 50 h, changes are detected in the morphology and dispersion of copper and iron species. The microstructure is more homogeneous and metal particles appear well dispersed and in intimate contact with the fluorite component for CuFe-C and CuFe-CG. In contrast, the CuFe-CT system apparently suffers a lack of connection between particles, inhomogeneous morphology and high porosity.

Fig. 9 shows the electrical conductivity results for the bimetallic Cu–Fe systems as a function of temperature under 10% H_2 and under air. Under reducing conditions, CuFe-C and CuFe-CG samples show metallic behaviour, electrical conductivity decreasing with increasing temperature. This is most likely due to the linking of the metallic particles of Cu and Fe which tends to form a continuous network as can be seen in SEM micrographs
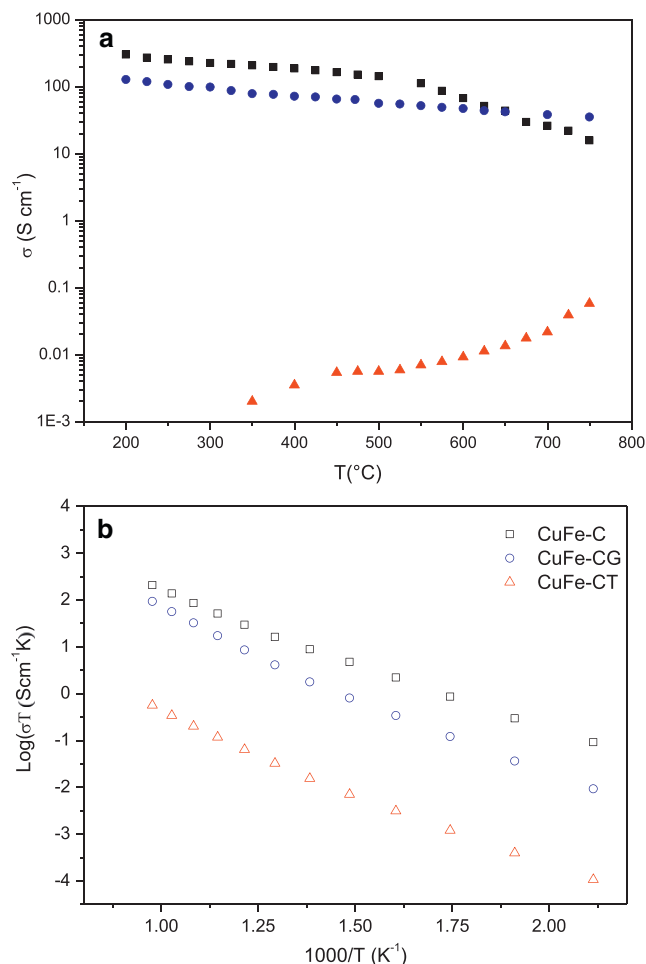

Fig. 9. Electrical conductivity of the bimetallic CuFe systems as function of temperature (200–750 °C): (a) under 10% H_2 and (b) under air.

(Fig. 8d and e). Under usual temperature conditions of an IT-SOFC anode (600–750 °C), CuFe-C displays conductivities values between 62.2 and 15.8 S cm^{-1} and CuFe-CG between 47.0 and 35.1 S cm^{-1}. In contrast, the CuFe-CT sample exhibits low conductivity values (0.01 and 0.06 S cm^{-1} at 600–750 °C, respectively) and semiconductor behaviour, the electrical conductivity increasing with increasing temperature. This implies an ionic-type conduction mechanism. This behaviour indicates discontinuous connections between metallic particles, as pointed out by SEM (Fig. 8e).

The Arrhenius plots obtained in air (Fig. 9b) revealed that the electrical conductivity of the samples decreases between around one and two orders of magnitude in the temperature range from 600 to 750 °C showing a semiconductor behaviour. The conductivity of the bimetallic CuFe systems appears thermally activated with activation energy of 0.59, 0.64 and 0.65 eV for CuFe-C, CuFe-CG and CuFe-CT, respectively.

4. Summary and conclusions

Different materials involving combinations of copper–iron with either ceria or Ce–Gd and Ce–Tb mixed oxides have been examined with respect to their structural and redox/catalytic properties towards oxidation of methane in the context of their potential application as anodes of SOFC for direct oxidation of hydrocarbons. CH_4-TPR results reveal important differences as a function of the presence of Gd or Tb in the systems. Thus, the doping of ceria by Gd or Tb is shown to be generally beneficial for the reactivity of

the materials towards methane as a consequence of the modifications induced in the catalytic/redox or transport properties of the materials. Differences in the methane reactivity as a function of the redox state of the catalyst are also revealed. As expected, the full oxidation process is favoured when the systems are oxidised while partial oxidation and/or methane cracking processes leading to carbon deposition prevail upon reduction of the materials produced during the course of thermal interaction with methane. The nature of such carbon deposits have been analysed by TPO, showing that their amount increases in the presence of Gd or Tb dopants in the fluorite phase of the supports. The beneficial effects on the methane activity observed in the presence of Tb or Gd dopants in ceria can be partly related to the stabilization of the fluorite phase in them, even after strong reduction under methane. In the absence of such dopants, a part of the iron and cerium react to give $CeFeO_3$ which could hinder redox activity of the system as a consequence of stabilization of such type of compound. Other processes taking place during reaction with CH_4 related to decoration of the metallic particles by reduced ceria – or doped ceria – subspecies, i.e. SMSI effects, as well as formation of core–shell (with iron forming the core) type particles are pointed out by XPS results, taking into account also XRD results for the samples reduced under CH_4. We cannot discard however, that some of these phenomena could be more simply related to screening effects as a consequence of carbon deposits formation more selectively onto metallic particles and among them on most reactive iron ones.

Except for the sample of undoped ceria in air, all compositions show thermal expansion coefficients, under both oxidizing and reducing atmospheres, which match well with TEC values typical for IT-SOFC electrolytes. The doping of ceria by Gd or Tb causes a reduction of particle size and a higher porosity which appears more pronounced for the sample with Tb with higher dopant concentration. In reducing atmosphere, the undoped and Gd-doped ceria formulations show a metallic behaviour and high electrical conductivity values. In contrast, the anode formulation doped with Tb presents semiconductor behaviour and a low electrical conductivity. This is probably due to the fact that its highest porosity hinders achievement of interconnection between metallic particles (as pointed out by SEM). XRD-based studies of the reactivity between solids revealed an excellent chemical compatibility between these materials and common IT-SOFC electrolytes, with the samples apparently undergoing similar structural modifications under both humidified hydrogen and methane.

Acknowledgements

References

[1] B.C.H. Steele, A. Heinzel, Nature 414 (2001) 345.
[2] B.C.H. Steele, J. Mater. Sci. 36 (2001) 1053.
[3] J.M. Ralph, A.C. Schoeler, M. Krumpelt, J. Mater. Sci. 36 (2001) 1161.
[4] S. McIntosh, R.J. Gorte, Chem. Rev. 104 (2004) 4845.
[5] G.M. Crosbie, E.P. Murray, D.R. Bauer, H. Kim, S. Park, J.M. Vohs, R.J. Gorte, SAE Paper 2001-01-2545, 2001.
[6] E.P. Murray, T. Tsai, S.A. Barnett, Nature 400 (1999) 649.
[7] S. Park, R.J. Gorte, J.M. Vohs, Appl. Catal. A 200 (2000) 55.
[8] A.-L. Sauvet, J. Fouletier, J. Power Sources 101 (2001) 259.
[9] S. Park, R. Craciun, J.M. Vohs, R.J. Gorte, J. Electrochem. Soc. 146 (1999) 3603.
[10] R. Craciun, S. Park, R.J. Gorte, J.M. Vohs, C. Wang, W.L. Worrell, J. Electrochem. Soc. 146 (1999) 4019.
[11] S. Park, J.M. Vohs, R.J. Gorte, Nature 404 (2000) 265.
[12] R.J. Gorte, S. Park, J.M. Vohs, C. Wang, Adv. Mater. 12 (2000) 1465.
[13] H. Kim, S. Park, J.M. Vohs, R.J. Gorte, J. Electrochem. Soc. 148 (2001) A693.
[14] R.J. Gorte, J.M. Vohs, R. Craciun, Patents WO 00/52780, US 2001/0029231 A1, US 2001/0053471 A1.
[15] R.J. Gorte, H. Kim, J.M. Vohs, J. Power Sources 106 (2002) 10.
[16] R.J. Gorte, J.M. Vohs, J. Catal. 216 (2003) 477.
[17] S. Jung, C. Lu, H. He, K. Ahn, R.J. Gorte, J.M. Vohs, J. Power Sources 154 (2006) 42.
[18] C. Sun, U. Stimming, J. Power Sources 171 (2007) 247.
[19] Z. Xie, W. Zhu, B. Zhu, C. Xia, Electrochim. Acta 51 (2006) 3052.
[20] M. Fernández-García, A. Martínez-Arias, J.C. Hanson, J.A. Rodriguez, Chem. Rev. 104 (2004) 4063.
[21] A. Martínez-Arias, A.B. Hungría, M. Fernández-García, A. Iglesias-Juez, J.C. Conesa, G.C. Mather, G. Munuera, J. Power Sources 151 (2005) 43.
[22] A. Hornés, D. Gamarra, G. Munuera, J.C. Conesa, A. Martínez-Arias, J. Power Sources 169 (2007) 9.
[23] A. Hornés, D. Gamarra, G. Munuera, A. Fuerte, R.X. Valenzuela, M.J. Escudero, L. Daza, J.C. Conesa, P. Bera, A. Martínez-Arias, J. Power Sources 192 (2009) 70.
[24] A. Martínez-Arias, M. Fernández-García, V. Ballesteros, L.N. Salamanca, J.C. Conesa, C. Otero, J. Soria, Langmuir 15 (1999) 4796.
[25] R. Hesse, T. Chassé, R. Szargan, Fresenius J. Anal. Chem. 365 (1999) 48.
[26] A. Martínez-Arias, M. Fernández-García, A.B. Hungría, J.C. Conesa, G. Munuera, J. Phys. Chem. B 107 (2003) 2667.
[27] A. Trovarelli, in: A. Trovarelli (Ed.), Catalysis by Ceria and Related Materials, Imperial College Press, 2002, p. 15, Chapter 2.
[28] A.B. Hungría, A. Martínez-Arias, M. Fernández-García, A. Iglesias-Juez, A. Guerrero-Ruiz, J.J. Calvino, J.C. Conesa, J. Soria, Chem. Mater. 15 (2003) 4309.
[29] J.R. McBride, K.C. Hass, B.D. Poindexter, W.H. Weber, J. Appl. Phys. 76 (1994) 2435.
[30] W.H. Weber, K.C. Hass, J.R. McBride, Phys. Rev. B 48 (1993) 178.
[31] T. Valdés-Solís, P. Tartaj, G. Marbán, A.B. Fuertes, Nanotechnology 18 (2007) 145603.
[32] J.F. Xu, W. Ji, Z.X. Shen, W.S. Li, S.H. Tang, X.R. Ye, D.Z. Jia, X.Q. Xin, J. Raman Spectrosc. 30 (1999) 413.
[33] X. Gao, J. Shen, Y. Hsia, Y. Chen, J. Chem. Soc. Faraday Trans. 89 (1993) 1079.
[34] D.L. Trimm, Catal. Today 37 (1997) 233.
[35] C.H. Bartholomew, Appl. Catal. A 212 (2001) 17.
[36] P. Wang, E. Tanabe, K. Ito, J. Jia, H. Morioka, T. Shishido, K. Takehira, Appl. Catal. A 231 (2002) 35.